Publ. Astron. Soc. Japan (2019) 71 (1), 10 (1–20)
doi: 10.1093/pasj/psy123
Advance Access Publication Date: 2018 November 22

Galactic foreground of gamma-ray bursts from AKARI Far-Infrared Surveyor

L. Viktor Toth,[1,2,*] Yasuo Doi,[3] Sarolta Zahorecz,[4,5] Sandor Pinter,[1,6] Istvan I. Racz,[1,2,6] Zsolt Bagoly,[7] Lajos G. Balazs,[1,2] Istvan Horvath,[6] Csaba Kiss,[2] Tímea Kovács,[1] and Toshikazu Onishi[4]

[1]Department of Astronomy, Eötvös Loránd University, Pázmány Péter sétány 1/A, H-1117 Budapest, Hungary
[2]Konkoly Observatory, Research Center for Astronomy and Earth Sciences, Hungarian Academy of Sciences, Konkoly Thege Miklós út 15-17, H-1121 Budapest, Hungary
[3]Department of Earth Science and Astronomy, Graduate School of Arts and Sciences, The University of Tokyo, 3-8-1 Komaba, Meguro-ku, Tokyo 153-8902, Japan
[4]Department of Physical Science, Graduate School of Science, Osaka Prefecture University, 1-1 Gakuen-cho, Naka-ku, Sakai, Osaka 599-8531, Japan
[5]National Astronomical Observatory of Japan, National Institutes of Natural Science, 2-21-1 Osawa, Mitaka, Tokyo 181-8588, Japan
[6]National University of Public Service, 1083 Budapest, Hungary
[7]Department of Physics of Complex Systems, Eötvös Loránd University, Pázmány Péter sétány 1/A, H-1117 Budapest, Hungary

*E-mail: l.v.toth@astro.elte.hu

Received 2018 August 24; Accepted 2018 October 5

Abstract

We demonstrate the use of the AKARI FIS All-Sky Survey maps in the study of extragalactic objects. A quick but reliable estimate of the Galactic foreground is essential for extragalactic research in general. We explored the galactic foreground and calculated hydrogen column densities using AKARI FIS and other recent all-sky survey data, and compared our results to former estimates. Our AKARI-FIS-based foreground values were then used toward gamma-ray burst (GRB) sources as input for X-ray afterglow spectrum fitting. From those fits the intrinsic column densities at the GRB sources were derived. The high-angular-resolution AKARI-FIS-based Galactic foreground hydrogen column densities are statistically very similar, but for most of the tested directions somewhat lower than previous estimates based on low-resolution data. This is due to the low filling factor of high-density enhancements in all galactic latitudes. Accordingly, our AKARI-FIS-based new intrinsic hydrogen column densities are usually higher or similar compared to the values calculated based, e.g., on the low-resolution Leiden/Argentine/Bonn survey data and listed in the Leicester database. The variation, however, is typically smaller than the error of the estimate from the fits of the X-ray afterglow spectra. There are a number of directions where the improvement of the foreground estimates resulted in an overestimate of magnitude or higher increment of the derived intrinsic hydrogen column densities. We concluded that most of the GRBs with formerly extremely low intrinsic

hydrogen column densities are in fact normal, but we confirmed that GRB050233 is indeed a non-enveloped long GRB.

Key words: gamma-ray burst: general — intergalactic medium — ISM: structure

1 Introduction

It is always a challenge to accurately estimate the column density of the galactic foreground interstellar medium in the direction of extragalactic sources. It is also one of the important parameters when calculating the physical parameters of gamma-ray burst (GRB) host galaxies. We started an investigation of the infrared sky brightness towards GRBs using AKARI Far-Infrared Surveyor (FIS: Kawada et al. 2007) all-sky maps.

GRBs are the most energetic explosions in the Universe, produced either when a very massive star undergoes core collapse, or when a double neutron star or a neutron star and a black hole binary merges (Woosley & Bloom 2006; Kumar & Zhang 2015). The duration of the gamma-ray emission is measured as the time interval during which a given fraction of the total observed counts have been detected. The T90 duration parameter is the time in seconds over which a burst emits from 5% of its total measured counts to 95%. In a simplified way GRBs are sorted, according to the duration of their gamma-ray emission, into short and long types with average durations (T90) of 0.3 s and 30 s, respectively (Kouveliotou et al. 1993). Additional types are intermediate (Horváth 2009; Horváth & Tóth 2016) and ultra-long (Boër et al. 2015) GRBs. Long-duration GRBs are associated with the explosions of massive stars (see, e.g., Stanek et al. 2003), while short ones are associated with binary mergers.

The redshift distribution of Swift GRBs (Gomboc 2012) shows that these objects may provide information on galaxy evolution, star formation history, and the intergalactic medium (IGM) up to high z values. A number of parameters of the GRBs and their host galaxies may be calculated from their X-ray and optical afterglows, which can outshine the brightest quasars—see, e.g., Zhang, Lü, and Liang (2016) for the GRB observational parameters, and Zhang et al. (2011) for the spectral components of the afterglow. The afterglow emission of GRBs is modeled as synchrotron radiation arising from the shock produced when the GRB jet impacts the surrounding medium (e.g., Mészáros & Ries 1997; Sari et al. 1998). Continuum afterglow radiation is expected in all wavelengths from X-ray to radio; however, sometimes not all are detected ("dark GRBs"). The afterglow X-ray spectrum may be approximated by a power-law continuum deformed by absorption from line-of-sight gas in the Milky Way and outside. The extragalactic absorption may be partly due to intergalactic clouds and the host galaxy ISM (intrinsic). A recent review of the absorption of H I and other lines is given by Schady (2015); see also Behar et al. (2011), Schady et al. (2011), Watson (2011), Zafar et al. (2011), and Campana et al. (2012), and references therein.

The literature of extragalactic absorption studies of GRBs is quite rich. When successfully measured, the afterglow spectrum also shows hydrogen and dust in the immediate intrinsic ISM at the GRB. Fynbo et al. (2009) used optical afterglow spectra to derive $N(\mathrm{H})_{\mathrm{int}}$ intrinsic hydrogen column densities for 33 GRBs. Elíasdóttir et al. (2009) detected red-shifted UV dust features in the afterglow optical spectrum. The intrinsic hydrogen column densities are typically significant: Campana et al. (2012) derived a mean value of $\log[N(\mathrm{H})_{\mathrm{int}}\,\mathrm{cm}^{-2}] = 21.7 \pm 0.5$.

Starling et al. (2013) found an apparent correlation between the redshift z and the so-called equivalent column density of extragalactic hydrogen, assuming it to be at the GRB's redshift. According to Wang (2013), part of the X-ray column density excess could be explained by photoelectric absorption due to diffuse intergalactic medium (IGM) or intervening absorbing clouds. A near-infrared probe by Totani et al. (2014) showed an indication of absorption made by neutral hydrogen in the diffuse intergalactic medium in the direction of the distant ($z = 5.9$) GRB130606A.

Correction for galactic foreground extinction may be based on various measurements, such as galaxy counts (Burstein & Heiles 1982); deriving extinction from H I 21 cm surveys, e.g., Kalberla et al. (2005); using extinction maps calculated from infrared surveys, e.g., Schlegel, Finkbeiner, and Davis (1998) and Schlafly and Finkbeiner (2011); or from spectroscopic measurements and colors of nearby Galactic stars. A low-resolution but still used all-sky map of the Galactic hydrogen column density was created by Dickey and Lockman (1990), who merged several surveys and averaged into 1 degree^2 bins in a galactic grid. A dust extinction map with $5'$ resolution has been calculated by Kohyama et al. (2013) for high ecliptic latitudes ($\beta > 30$) from IRAS and COBE/DIRBE data.

Willingale et al. (2013) presented a revision of the Galactic absorption calculations using an empirical method investigating 493 afterglows detected by the Swift X-ray Telescope (XRT). The $N(\mathrm{H})_{\mathrm{Gal}}$ Galactic foreground hydrogen column density was calculated based on a

low-angular-resolution H I 21 cm survey combined with the reddening of Schlegel, Finkbeiner, and Davis (1998) (SFD).

Recently, several of the GRB hosts were probed for far-infrared (FIR) emission using the Herschel Space Telescope by, e.g., Schady et al. (2014) and Hunt et al. (2014). They did not discuss the related extended foreground FIR emission, and took the galactic dust reddening values from Schlafly and Finkbeiner (2011).

To interpret spectral line measurements one needs metallicity information. According to, e.g., Yoon, Langer, and Norman (2006), long GRBs preferably occur in metal-poor environments. We note that in spite of that, Elliott et al. (2013) derived a solar metallicity in the host galaxy of GRB110918A and Schady et al. (2015) derived a super-solar metallicity in the host galaxy of GRB130925A (an ultra-long GRB). It is fair to say that GRBs reside in varied environmental conditions. Investigating GRBs with various redshifts, Zafar (2016) concluded that the dust-to-metals ratios are surprisingly close to the Galactic value, and derived a total selective extinction ratio of $R_V = 2.66$. The spectra of afterglows probe the immediate environment of GRBs, which is highly diverse as shown by Wiseman et al. (2017) using VLT X-shooter measurements. They also discussed the degeneracy of gas phase metallicity and depletion strength factor.

Because the X-ray afterglows are bright and have simple continuum spectra, they provide an excellent opportunity to study the cold absorbing material in the distant host galaxies, and this is what turned our attention to them. We do not try to discuss the problem of X-ray afterglow spectrum modeling in its full complexity, but we call attention to the substructure of the Galactic foreground ISM, and investigate how a better-resolved foreground extinction affects the estimates of intrinsic hydrogen column densities.

We make use of recent all-sky surveys like HI4PI, i.e., the recent merger of the EBHIS and GASS surveys (HI4PI Collaboration 2016), and the Planck sky survey estimating the Galactic foreground. Then we will demonstrate the use of a much higher-resolution data set, the AKARI FIS, resolving the foreground.

Section 2 will describe the various input data and their reduction. Then we will introduce the new calibrated high-resolution AKARI-based Galactic column density maps, and the revised column densities. The consequences will be discussed in the final section.

2 Input data and data analysis

2.1 GRB sample selection

Modeling afterglow X-ray spectra modulated also by the absorption caused by the intrinsic ISM naturally requires a knowledge of the precise redshift values of the hosts. The accuracy of the fit also depends on the quality of the X-ray spectra, which we investigated for 326 SWIFT-discovered GRBs with known spectrometric redshifts (Horváth et al. 2015; Bagoly et al. 2016). The input sample was narrowed in two steps based on the online available data in the UK Swift Science Data Centre database (Evans et al. 2009) and the quality of the available infrared maps toward the direction of the selected GRBs. Each Swift XRT light curve contains a maximum of 100 bins, where each bin contains the observed count rate in one frame of data. The bin integration time varies across the lightcurve and is set to the frame exposure for the different modes. In the first step we dropped GRBs with less than 21 bins (i.e., the first quantile of the lightcurve length distribution). We ordered the remaining 252 GRBs according to the average photon rate (photons s^{-1}) and according to the total X-ray fluence. The two ranks were summed for each GRB. We selected the top 126 sources, cutting the sample where a sharp drop was visible in the histogram of the ranks. A few sources with lower but still acceptable-quality ranks were added, for which Herschel data (L. V. Toth et al. in preparation) was available. We also added GRB051022, discovered by HETE (High Energy Transient Explorer: Price et al. 1992), and GRB130702A discovered by Fermi; both were also well detected by Swift XRT. GRB051022 is an LGRB with a well-studied host galaxy in the Giant GRB ring (Balazs et al. 2015). GRB130702A (also known as SN 2013dx) is one of the well-known supernova GRBs. The resulting sample of 162 GRBs was further narrowed based on the quality of the available AKARI far-infrared data; see the details in subsections 2.4 and 3.1.

Figure 1 shows the $N(\mathrm{H})_{\mathrm{Gal}}$ galactic vs. $N(\mathrm{H})_{\mathrm{int}}$ intrinsic hydrogen column density values for the 326+2 SWIFT XRT GRBs with black symbols: (+) for short, (diamonds) for intermediate, (X) for long, and (*) for unclassified GRBs.

2.2 Planck PR2 maps

Planck Collaboration (2016) combined the Planck all-sky maps with Infrared Astronomical Satellite (IRAS: Neugebauer et al. 1984) and Wide-field Infrared Survey Explorer (WISE: Wright et al. 2010) maps to explore the dust thermal emission from the Milky Way ISM with greater spatial resolution and frequency coverage than ever before in the wavelength range of $10\,\mu\mathrm{m} < \lambda < 970\,\mu\mathrm{m}$. We have used $0.^{\circ}5 \times 0.^{\circ}5$-sized dust extinction maps[1] from Planck PR2 to investigate the Galactic foreground with $5'$ resolution in the direction of the GRBs, and to check the calibration of the AKARI all-sky maps. The hydrogen column density was calculated as $N(\mathrm{H}) = 2.2 \times 10^{21} \times A_v$. Two extinction maps in the visible V band are available:

[1] COM_CompMap_Dust-DL07-AvMaps_2048_R2.00.fits.

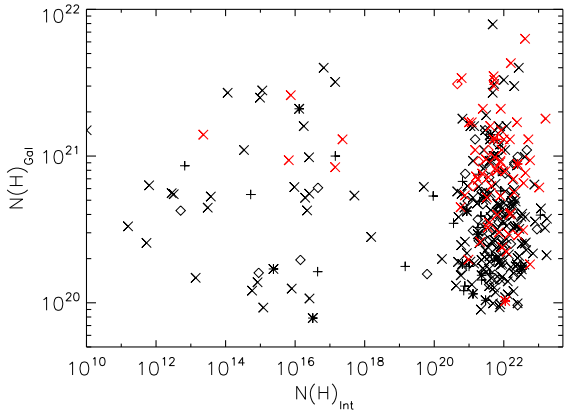

Fig. 1. Galactic vs. intrinsic N(H) column density values for the SWIFT XRT GRBs with known spectrometric redshifts based on the Leicester database. Red symbols indicate the selected sources in our narrowed sample with high correlation coefficient. Plus signs, diamonds, crosses, and asterisks indicate the short, intermediate, long, and not classified GRBs, respectively. Note the high number of non-enveloped GRBs (i.e., where $N(H)_{int} < 10^{18}$ cm^{-2}; see subsection 4.2).

(i) the value from the model, A_v(DL), and (ii) the renormalized one, A_v(RQ), which matches extinction estimates for quasars (QSOs) derived from the Sloan digital sky survey (SDSS) data. We used the A_v(RQ) maps in this study.

2.3 Other archival data

As a typical method for processing extragalactic X-ray data, we also used the Leiden/Argentine/Bonn (LAB) survey (Kalberla et al. 2005), which has an angular resolution of 36′. That is also the standard procedure applied by the UK Swift Science Data Centre[2] (UKSSDC) to take into account the contribution of the Galactic foreground.

We also utilized the most recent H I all-sky survey data archive known as HI4PI (HI4PI Collaboration 2016), which combined the southern GASS (Parkes Galactic All Sky Survey: McClure-Griffiths et al. 2009) and the northern EBHIS (Effelsberg–Bonn H I Survey of Milky Way gas: Winkel et al. 2016) surveys with a uniform resolution of 16.′2.

In order to give the reader the possibility of comparison we also present the Planck first Public Release (PR1: Planck Collaboration 2014a) column density distributions in the Supplementary Material. Finally, we make use of the reddening maps of Schlafly and Finkbeiner (2011) as well.

2.4 Analysis of the AKARI FIS All-Sky Survey images

The Japanese AKARI satellite for infrared astronomical purposes operated with a telescope of 68.5 cm in diameter (Murakami et al. 2007). The telescope and focal plane instruments were cooled to a temperature lower than 6 K in a liquid-helium cryostat (Nakagawa et al. 2007) to avoid the thermal emission of the instruments. The Far Infrared Surveyor (FIS) is one of the two focal plane instruments on board (Kawada et al. 2007). Four photometric bands were used to scan the infrared sky between 50 and 180 μm. Detectors and bands are the following: *N60* (65 μm), *WIDE-S* (90 μm), *WIDE-L* (140 μm), and *N160* (160 μm).

Doi et al. (2012, 2015) have processed full-sky images of the AKARI FIR survey at 65 μm, 90 μm, 140 μm, and 160 μm. The images achieve a detection limit of $<$10 MJy sr^{-1} with absolute and relative photometric accuracies of $<$20%. The spatial resolution of the AKARI FIR survey is 1′–2′. Among the four wavebands, the 90 μm and 140 μm bands continuously cover the 50–180 μm wavelength range, which corresponds to the peak of the dust thermal emission. We can thus evaluate color temperature and dust column density from the AKARI FIR survey with high spatial resolution. Ootsubo et al. (2016) successfully estimated the dust band component of the Zodi emission using AKARI images. We used the new Zodi-subtracted images, where the residual of the Zodi component is $<$0.5 MJy sr^{-1} in the 90 μm image and $<$0.1 MJy sr^{-1} in the 140 μm image.

We subtracted 30 by 30 arcmin^2 images centered on the 162 GRBs selected in subsection 2.1. Data quality was checked with the use of the AKARI error maps, scan coverage maps, and comparison with Planck maps.

2.5 Column density estimation

The color temperature (T_{dust}) maps and the dust extinction (τ) maps of the large grain emission were estimated using the 90 μm and 140 μm intensity images. Planck Collaboration (2014b) made a full-sky dust map with 5′ spatial resolution by fitting Planck 353 GHz, 545 GHz, 857 GHz, and IRAS 100 μm data with modified black body (MBB). They calibrated their dust maps with interstellar extinction values observed for SDSS QSOs and proposed to use radiance ($\mathcal{R}$), or integrated flux of MBB, as an indicator of the interstellar extinction as $\mathcal{R}$ shows the best correlation with the SDSS interstellar extinction. The radiance $\mathcal{R}$ is evaluated by the following equation (Planck Collaboration 2014b):

$$\mathcal{R} = \int_\nu I_\nu d\nu = \int_\nu \tau_{\nu_0} B_\nu(T_{dust}) d\nu \left(\frac{\nu}{\nu_0}\right)^\beta$$
$$= \tau_{\nu_0} \frac{\sigma_S}{\pi} T_{dust}^4 \left(\frac{kT_{dust}}{h\nu_0}\right)^\beta \frac{\Gamma(4+\beta)\zeta(4+\beta)}{\Gamma(4)\zeta(4)}, \quad (1)$$

[2] ⟨http://www.swift.ac.uk/⟩.

where β is the spectral index, σ_S is the Stefan–Boltzmann constant, k is the Boltzmann constant, h is the Planck constant, Γ is the Gamma function, and ζ is the Riemann zeta function. Planck Collaboration (2014b) calibrated their estimated $\mathcal{R}$ with the SDSS interstellar extinction and scaled their $\mathcal{R}$ to $E(B-V)$ as $E(B-V) = 5.4 \times 10^5 \times \mathcal{R}$. We followed their discussion and estimated the $\mathcal{R}$ value with 2′ spatial resolution by applying equation (1) to our AKARI dust maps. The H I column density was calculated with the following equation (Güver 2009):

$$N(\mathrm{H}) = 6.86 \times 10^{21}\ \mathrm{cm}^{-2}\ E(B-V). \quad (2)$$

2.6 Modeling Swift XRT X-ray spectra

We investigated the X-ray spectra of GRBs observed by the X-Ray Telescope (XRT) of the Swift satellite. High-level data products, such as lightcurves and spectra of the GRB afterglows, are created automatically for all the Swift-XRT-observed GRBs by the "Swift-XRT team" using software tools of HEAsoft v6.22[3] (Evans et al. 2009). In most cases several spectral data sets exist for each GRB. The XRT has two different observing modes, photon counting (PC) and windowed timing (WT) modes. For each mode, the default is a "time-averaged" spectrum, which is built from all the observations obtained within 12 hr of the first observation of a GRB. The spectra during different "phases" of the XRT lightcurves are also provided by the UKSSDC.

The most important physical parameters of the afterglows are also calculated, and published along with the high-level data products at the UKSSDC web site. We downloaded XRT spectra from their database. We then analyzed the spectra using the Xspec[4] (Arnaud 1996; Dorman & Arnaud 2001) command-driven, interactive, X-ray spectral-fitting software. We adopted an updated version (Xspec 12.9.1) of the procedure used by Evans et al. (2009) to model the spectra.

The fitted model was an absorbed power law with two absorption components described by two functions. The first component, called "tbabs," takes the Galactic foreground into account, with a fixed Galactic hydrogen column density (calculated from an input parameter) at $z = 0$. The second component, called "ztbabs," describes the extragalactic absorption (assumed to be dominated by the host galaxy of the GRB) at a given redshift value. The extragalactic hydrogen column density is a fitted parameter. These function names refer to the Tuebingen–Boulder absorption model described and implemented in Xspec by Wilms, Allen, and McCray (2000). We need to set the abundances of the interstellar medium and also the photoionization cross sections of the different absorbers. The abundances are also given by Wilms, Allen, and McCray (2000), and the cross sections are given by Verner et al. (1996).

As a starting point, we used the original Xspec scripts from the database. The Xspec software can use several minimization methods and objective functions (statistics) for the fit, for example χ^2 statistics or C-statistics. We applied the default minimization method, which is the modified Levenberg–Marquardt algorithm based on the CURFIT routine from Bevington (1969), and ran Xspec with the "cstat" option (i.e., using C-statistics).

We used the Wilms, Allen, and McCray (2000) abundance models and the "vern" photoelectric absorption cross-section from Verner et al. 1996. We set the cosmological parameters as $H_0 = 70\,\mathrm{km\,s^{-1}\,Mpc^{-1}}$, $\Lambda_0 = 0.73$, and the deceleration parameter $q_0 = 0.0$. We also set the redshift (for the extragalactic absorber) and the photon index of the power law.

Unlike the original "Leicester script" (see Willingale et al. 2013), we used various data sets (see later) calculating the Galactic foreground and applied that as input for Xspec. The remaining free parameter to fit was the $N(\mathrm{H})_{\mathrm{int}}$ intrinsic hydrogen column density. Its typical error from the fit varies between $10^{21}\,\mathrm{cm}^{-2}$ and $10^{22}\,\mathrm{cm}^{-2}$. We note here that the relative error of $N(\mathrm{H})_{\mathrm{int}}$ is too high (orders of magnitude) for too small values. Thus for $N(\mathrm{H})_{\mathrm{Gal}} < 10^{18}\,\mathrm{cm}^{-2}$ we only give upper limits.

3 Results

3.1 Calibrated AKARI column density maps

$N(\mathrm{H})_{\mathrm{Gal}}$ column density maps were calculated based on LAB, SFD, HI4PI, Planck PR1, Planck RQ, Planck DL, and AKARI maps at the resolutions of 5′, 7′, 11′, and 36′. Figure 2 shows the galactic foreground hydrogen column density distribution in the direction of GRB140213A, based on the mentioned all-sky surveys at different resolutions. The images in the top row show a larger area, while the images in the middle and bottom rows show the central area of the top row (marked with a white box) with higher angular resolution. Such sets of images are available for all our selected targets in the supplementary data to this article.

Figure 3 shows the correlation plots of the estimated galactic foreground hydrogen column densities in the direction of GRB140213A, based on various all-sky surveys. The top row, from left to right, shows AKARI vs. Planck PR1, AKARI vs. Planck PR2 RQ, AKARI vs. Planck PR2 DL, and SFD vs. AKARI. The bottom row shows LAB survey vs. Planck PR1, LAB survey vs. Planck PR2 RQ, LAB survey

[3] ⟨https://heasarc.nasa.gov/docs/software.html⟩.

[4] Xspec is part of the HEAsoft software package of NASA's High Energy Astrophysics Science Archive Research Center (HEASARC), available at ⟨http://heasarc.gsfc.nasa.gov/lheasoft/download.html⟩.

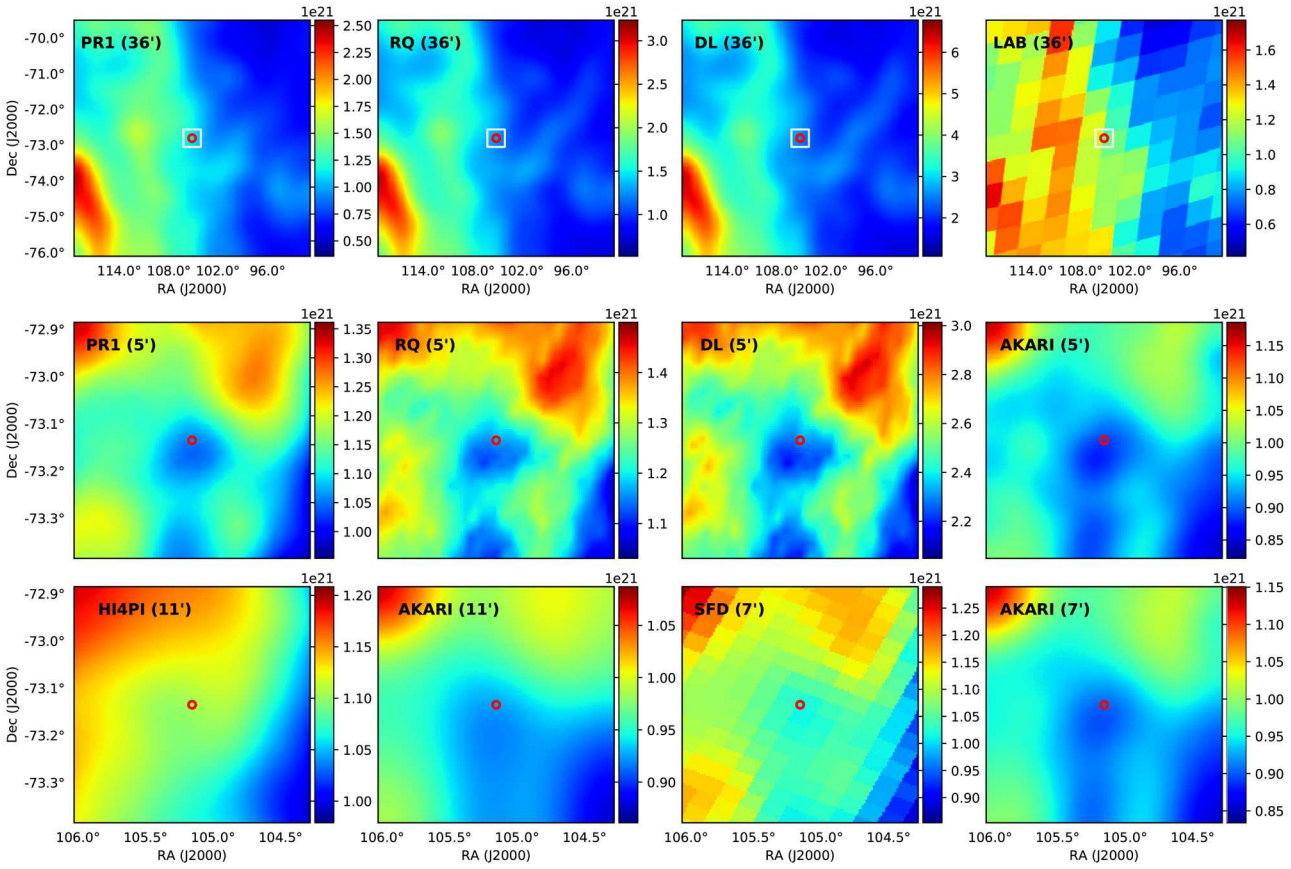

Fig. 2. Galactic foreground hydrogen column density distribution in the direction of GRB140213A, based on various all-sky surveys. First row: The first three images from the left are Planck PR1, Planck PR2 RQ, and Planck PR2 DL-based $N(\mathrm{H})_{\mathrm{Gal}}$ distributions smoothed to 36′ resolution; the right one is the $N(\mathrm{H})_{\mathrm{Gal}}$ from the LAB survey. Second row: All images show the central area of the top row (marked with a white box), but with a resolution of 5′. The first three images from the left are similar to the first row; the left one is based on AKARI FIS data. Third row: The first two from the left are $N(\mathrm{H})_{\mathrm{Gal}}$ with 11′ resolution based on EBHIS and AKARI. The right two are based on the SFD and AKARI, both with 7′ resolution. See also text.

vs. Planck PR2 DL, EBHIS vs. AKARI. The Pearson correlation coefficient between the Planck PR2 and AKARI values is 0.91 for this example source. More than one third of the selected sources have similarly high linear correlation.

To check the calibration of the AKARI maps, the Planck RQ and AKARI column density maps were sampled on a 5 × 5 grid for the 0.°5 × 0.°5 regions. From our initial sample of 162 sources with AKARI maps, we have selected the regions with a Pearson correlation coefficients above 0.51—see figure 4 for the distribution of the Pearson coefficients of the final sample of 69 sources. The median value of the Pearson coefficient is 0.80. Table 1 shows the basic parameters [ID, coordinates, redshift, and foreground $N(\mathrm{H})$] of the final sample.

Figure 5 shows a comparison of the Planck RQ and calibrated AKARI column density values sampled on the 5 × 5 grid for the final sample. The Pearson correlation coefficient is 0.9979. The selected regions cover a broad range in column density between 5×10^{19} and $1.5 \times 10^{22}\,\mathrm{cm}^{-2}$ values.

The distributions of the galactic latitude, galactic longitude, and redshift of the 69 selected sources were compared to the initial input sample with the Wilcoxon rank sum test with continuity correction. The results are shown in figure 6. The H_0 hypothesis that the 69 selected sources are a representative sample of the initial data was rejected in the case of galactic latitude distribution with p-value 0.006, but cannot be rejected for the galactic longitude and redshift where the p-values are 0.168 and 0.080, respectively. Apparently we oversampled the sources with redshift above 3 and with low galactic latitudes.

3.2 Structure of the FIR foreground

The calibrated AKARI-based column density maps are shown with 2′ resolution in the Appendix. The maps are centered on the GRB's position.

In order to illustrate the typical patterns of $N(\mathrm{H})_{\mathrm{Gal}}$, we have selected four GRBs. Figure 7 shows the striking effect of high spatial resolution, where we compared the column

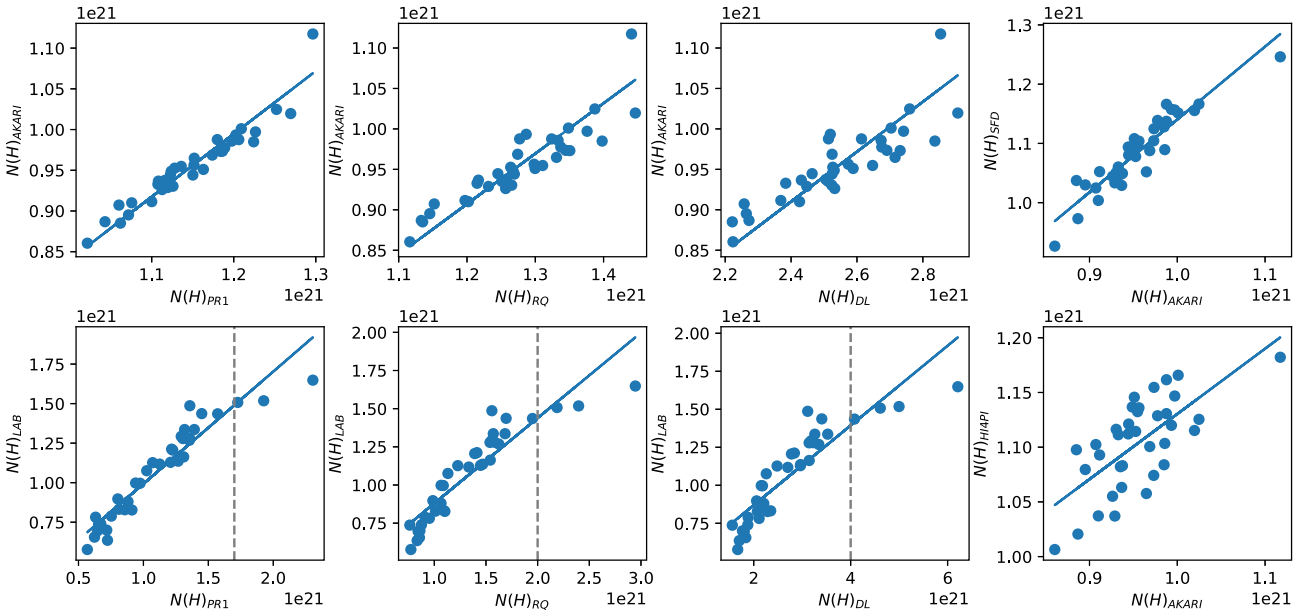

Fig. 3. Correlation plots of the estimated galactic foreground hydrogen column densities in the direction of GRB140213A, based on various all-sky surveys. Top row from left to right: AKARI vs. Planck PR1, AKARI vs. Planck PR2 RQ, AKARI vs. Planck PR2 DL, SFD vs. AKARI. Bottom row: LAB survey vs. Planck PR1, LAB survey vs. Planck PR2 RQ, LAB survey vs. Planck PR2 DL, EBHIS vs. AKARI. Ordinary least-squares fitted lines are drawn. The Pearson's correlation coefficients and the least-squares fits were calculated only at the linear parts of the correlation plots with HI data; the limits are indicated with dashed lines.

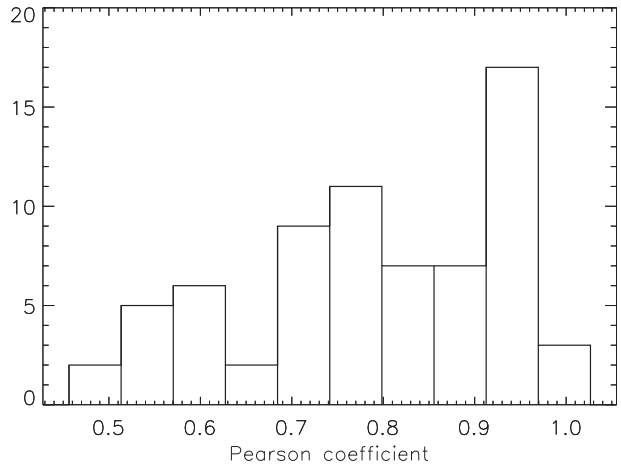

Fig. 4. Histogram of the Pearson coefficient for the 69 selected sources.

density distributions based on the LAB survey data, Planck PR2 RQ data, and AKARI FIS maps. The maps also show interesting patterns, which are sort of typical.

GRB140213A, a long GRB, is seen inside a void in the AKARI-based image, while it is on the edge of an extended H I cloud in the LAB survey. The difference in the apparent patterns is clearly due to the different resolutions. These are highly linearly correlated after smoothing the data sets to the same resolution.

GRB131004A, a short GRB, is in the direction of a filamentary cloud, another typical structure of the foreground, while it is just a low-column-density region in the LAB. Here we note that the bad correlation between the H I and far-infrared-based Galactic foreground column densities is most possibly due to the presence of molecular gas. The direction of GRB131004A is next to the dark cloud TGU L21 catalogued by Dobashi et al. (2005).

GRB100219A, a long GRB, is also inside a void in our high-resolution AKARI foreground, while it is seen in the direction of an H I cloud in the LAB survey. The various foreground estimations are well correlated.

GRB061126, a long GRB, is seen at the edge of an extended diffuse structure in each survey. That cloud may be related to the H II region LBN 148.83+17.71 (or LBN 700; Lynds 1965). We see good linear correlations in spite of the relatively high hydrogen column densities.

3.3 Analysis of the pattern of the foreground

A simple test of the pattern is counting high and low column density pixels in the target fields. We calculated the ΔN dynamical range of foreground hydrogen column density for each field as $\Delta N = \max[N(\mathrm{H})_{\mathrm{Gal}}] - \min[N(\mathrm{H})_{\mathrm{Gal}}]$. Then we defined the low column density pixels where $N(\mathrm{H})_{\mathrm{Gal}} < 1/3\Delta N + \min[N(\mathrm{H})_{\mathrm{Gal}}]$, and the high column density pixels where $N(\mathrm{H})_{\mathrm{Gal}} > 2/3\Delta N + \min[N(\mathrm{H})_{\mathrm{Gal}}]$. The filling factor of low and high column density pixels is the number of such pixels divided by the total pixel number of the field (14400 in our case). Histograms of the fields with various filling factors are plotted in figure 8.

Table 1. Basic parameters of the 69 selected GRBs.*

ID	RA [h m s]	Dec [° ′ ″]	z	$N(H)_{Gal}$ [10^{20} cm^{-2}]						α
				S&F	LAB	HI4PI	RQ	AKARI	Mean	
GRB050219A	11:05:38.99	−40:41:03.00	0.211	8.53	8.41	7.14	9.41	9.35	10.46	−4.54
GRB050223	18:05:32.20	−62:28:20.40	0.592	5.38	6.21	6.25	6.20	6.28	6.95	−4.32
GRB050318	03:18:51.15	−46:23:43.70	1.444	1.23	1.60	1.45	1.43	1.68	4.07	−3.66
GRB050730	14:08:17.09	−03:46:18.90	3.969	3.44	3.50	2.97	3.57	3.70	4.29	−3.47
GRB050820A	22:29:38.12	19:33:37.00	2.614	3.01	4.25	4.01	3.54	4.03	11.07	−4.88
GRB050904	00:55:04.80	14:11:20.40	6.295	4.31	4.99	4.51	4.43	1.73	9.30	−3.83
GRB051022	23:56:04.14	19:36:24.00	0.809	4.07	3.97	3.91	4.74	5.23	5.74	−4.38
GRB051109A	22:01:15.33	40:49:23.70	2.346	12.76	15.78	14.17	14.33	15.44	14.78	−4.48
GRB051111	23:12:33.17	18:22:28.80	1.549	10.93	5.54	5.88	10.26	9.88	15.55	−4.40
GRB060124	05:08:25.86	69:44:26.41	2.296	9.38	9.27	9.34	11.40	13.33	14.31	−4.92
GRB060729	06:21:31.85	−62:22:12.70	0.543	3.64	4.42	3.94	5.26	6.12	43.37	−4.66
GRB061126	05:46:24.46	64:12:38.50	1.159	12.55	10.72	10.42	14.61	18.31	20.39	−4.28
GRB061202	07:02:06.07	−74:41:54.69	2.254	10.26	11.40	10.46	11.85	11.81	17.19	−4.49
GRB061222A	23:53:03.45	46:31:57.70	2.088	7.00	9.41	8.91	8.39	8.05	20.28	−4.34
GRB070306	09:52:23.29	10:28:55.50	1.496	1.88	2.82	2.68	3.12	4.11	3.73	−4.33
GRB070328	04:20:27.68	−34:04:00.70	2.063	2.45	2.91	2.82	2.87	4.60	3.95	−3.76
GRB070419B	21:02:49.77	−31:15:48.70	1.959	6.17	6.68	5.37	6.23	6.68	5.27	−5.14
GRB070714B	03:51:22.23	28:17:51.20	0.923	9.72	6.64	6.94	9.94	11.99	24.79	−4.98
GRB071020	07:58:39.84	32:51:25.19	2.146	4.35	4.85	5.38	4.55	2.95	10.00	−3.78
GRB071025	23:40:17.08	31:46:42.50	5.200	5.05	4.88	4.86	5.14	4.13	9.56	−4.17
GRB080319C	17:15:55.49	55:23:30.60	1.950	1.78	2.60	2.18	2.88	2.69	2.59	−4.12
GRB080602	01:16:42.17	−09:13:55.90	1.820	1.89	3.57	2.93	1.85	1.61	1.74	−3.33
GRB080721	14:57:55.85	−11:43:24.54	2.591	6.97	6.90	7.53	8.55	9.22	5.71	−5.19
GRB080928	06:20:16.84	−55:11:58.95	1.692	4.54	5.32	4.71	5.14	5.43	8.84	−4.22
GRB081029	23:07:05.34	−68:09:19.81	3.848	2.12	2.64	2.70	2.17	2.04	2.77	−3.77
GRB090201	06:08:12.52	−46:35:25.00	2.100	4.60	5.62	4.78	6.80	7.23	5.51	−4.17
GRB090205	14:43:38.61	−27:51:10.40	4.650	8.03	7.43	7.43	9.38	7.59	9.89	−4.47
GRB090418A	17:57:15.17	33:24:21.10	1.608	2.99	3.04	3.30	3.67	4.36	7.26	−4.74
GRB090618	19:35:58.69	78:21:24.30	0.540	5.97	5.55	5.93	8.22	7.12	11.85	−3.97
GRB090809	21:54:43.19	−00:05:01.83	2.737	6.50	5.03	6.36	7.04	4.54	12.01	−4.00
GRB091024	22:36:57.60	56:53:05.99	1.092	66.63	44.18	48.63	77.18	76.93	92.92	−3.46
GRB100219A	10:16:48.54	−12:33:57.90	4.667	5.20	7.37	6.38	4.91	5.04	8.10	−3.70
GRB100606A	23:22:30.38	−66:14:28.80	1.555	1.85	2.40	2.41	1.99	1.50	4.50	−3.98
GRB100728A	05:55:01.99	−15:15:19.60	1.567	11.64	9.26	10.38	14.78	13.16	27.08	−3.88
GRB100728B	02:56:13.47	00:16:52.18	2.106	4.66	7.14	5.55	6.23	5.17	5.45	−3.96
GRB100901A	01:49:03.42	22:45:30.80	1.408	6.66	7.47	6.72	7.69	6.27	5.88	−5.09
GRB100906A	01:54:44.11	55:37:49.60	1.727	25.56	22.15	21.58	31.10	28.58	31.19	−4.40
GRB101225A	00:00:47.51	44:36:01.11	0.847	6.73	7.81	7.74	8.23	6.61	18.94	−5.00
GRB110213A	02:51:51.39	49:16:23.54	1.460	22.22	22.12	21.95	25.21	23.94	24.21	−3.95
GRB110715A	15:50:44.08	−46:14:06.52	0.820	41.71	24.53	28.09	48.10	50.10	43.34	−3.83
GRB110818A	21:09:20.87	−63:58:51.71	3.361	2.39	2.45	2.76	2.38	2.46	2.24	−4.37
GRB111107A	08:37:54.66	−66:31:12.29	2.893	9.06	9.21	9.30	12.44	12.16	20.72	−4.25
GRB111123A	10:19:23.13	−20:38:41.00	3.151	3.70	5.83	5.48	4.38	4.93	6.93	−3.91
GRB111228A	10:00:16.01	18:17:51.80	0.716	2.26	3.00	2.96	2.99	2.35	3.09	−4.00
GRB111229A	05:05:08.86	−84:42:39.10	1.381	12.34	10.46	9.37	14.76	17.58	17.49	−4.37
GRB120118B	08:19:29.04	−07:11:05.10	2.943	10.13	7.28	6.98	15.16	17.82	13.31	−4.37
GRB120326A	18:15:37.13	69:15:35.35	1.798	3.36	5.10	4.95	4.33	4.10	11.58	−3.55
GRB120404A	15:40:02.29	12:53:06.30	2.876	3.34	3.48	3.43	3.48	2.89	3.53	−3.83
GRB120729A	00:52:17.83	49:56:23.10	0.800	11.40	13.87	13.84	14.60	14.55	15.76	−4.25
GRB120802A	02:59:22.22	13:46:06.00	3.796	10.82	10.27	9.93	11.22	11.36	6.41	−4.60
GRB120811C	13:18:43.82	62:18:02.80	2.671	2.39	2.21	2.55	2.49	3.22	4.94	−3.42
GRB120907A	04:59:00.00	−09:18:54.00	0.970	6.29	4.50	5.22	6.73	7.22	5.16	−3.79
GRB120909A	18:22:56.77	−59:26:55.00	3.930	6.04	5.82	5.88	6.65	6.78	12.78	−4.54
GRB121024A	04:41:53.28	−12:17:26.80	2.299	6.88	5.21	5.36	6.40	5.86	10.51	−4.72

Table 1. (Continued)

ID	RA [h m s]	Dec [° ′ ″]	z	$N(H)_{Gal}$ [10^{20} cm^{-2}] S&F	LAB	HI4PI	RQ	AKARI	Mean	α
GRB121128A	20:02:24.00	54:17:59.10	2.200	20.98	21.46	19.90	25.51	27.08	28.92	−3.75
GRB130701A	23:48:55.08	36:06:01.51	1.155	5.83	6.59	7.04	6.33	7.00	5.57	−4.70
GRB130702A	14:29:14.77	15:46:26.50	0.145	2.89	1.83	1.79	2.27	2.52	2.74	−3.27
GRB130907A	14:23:34.04	45:36:27.10	1.238	0.78	0.98	0.93	0.85	1.00	2.09	−1.35
GRB131004A	19:44:27.10	−02:57:30.40	0.717	19.75	6.84	6.60	25.96	23.77	33.32	−4.18
GRB131227A	04:29:30.78	28:52:58.90	5.250	68.15	15.85	16.17	67.21	59.46	78.05	−3.47
GRB140206A	09:41:20.26	66:45:38.59	2.730	9.91	4.76	5.54	9.81	12.26	10.56	−4.05
GRB140213A	07:00:37.13	−73:08:13.51	1.208	10.21	10.76	11.04	11.67	10.99	15.35	−4.20
GRB140304A	02:02:34.26	33:28:25.70	5.283	5.32	5.82	6.03	6.04	6.54	8.41	−4.33
GRB140430A	06:51:44.61	23:01:25.20	1.602	9.39	16.15	14.86	14.52	13.03	19.68	−3.88
GRB140506A	18:27:06.05	−55:38:08.70	0.889	6.39	7.39	6.84	8.68	8.18	9.68	−4.25
GRB140614A	15:24:40.59	−79:07:43.60	4.233	8.46	7.75	8.27	9.63	10.49	14.52	−4.06
GRB140703A	00:51:58.97	45:06:06.90	3.140	7.80	9.16	9.38	8.32	9.26	17.94	−4.09
GRB141004A	05:06:56.14	12:49:11.30	0.573	21.52	18.76	18.97	21.36	22.59	19.98	−4.42
GRB150403A	20:46:01.15	−62:42:41.00	2.060	3.68	4.12	4.24	3.25	3.02	3.02	−3.95

*Columns: ID; RA and Dec (J2000.0) coordinates; redshift; various foreground column density estimates in the direction of the GRB based on Schlafly and Finkbeiner reddening; LAB H I survey; HI4PI; Planck RQ; AKARI data; the average column density calculated from AKARI data in an area of 0.°5 × 0.°5 around the GRB's position; the α Fourier spectral indices.

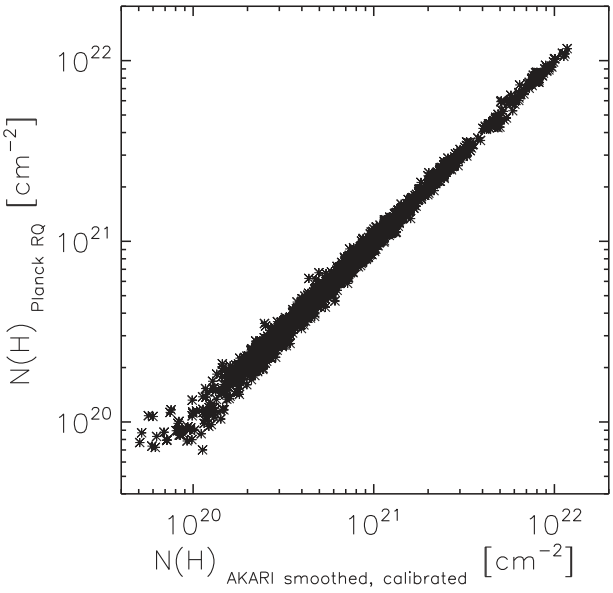

Fig. 5. Comparison of Planck RQ and calibrated AKARI-based column density maps at 5′ resolution for the 69 selected sources. The Pearson correlation coefficient is 0.9979.

As can be seen, the filling factor of low column density positions is typically larger than that of the high column density area in the studied small fields. That means that we have a higher possibility of overestimating the foreground column density when using low-resolution observations.

Fourier transformation of the AKARI N(H) maps was made by routines written in IDL based on the standard IDL FFT routine with periodogram normalization (Press et al. 1992). For all maps the highest spatial sampling frequency corresponds to the pixel size of the used AKARI images (120 × 120). The Nyquist limit that allows correct sampling (without aliasing) is half of that frequency (chapter 12.1 of Press et al. 1992), i.e., double the pixel size of the array. Therefore, the upper limit of the spatial frequency considered for the Fourier power spectrum was set to the Nyquist limit. Instead of averaging $P(f)$ fluctuation power values in annuli for each $f = |f|$ spatial frequency, we used all the individual data points [f, $P(f)$ pairs] to derive the final power spectrum. The spectral slope α is derived by robust line fitting to all data points in the log (f)–log (P) space. Three examples are shown with different galactic latitudes in figure 9.

Due to the similar primary mirror sizes and wavelength ranges of the AKARI FIS and ISO ISOPOHOT imaging instruments (for the latter, see Lemke et al. 1996), identical spatial structure is expected from both instruments for the same areas of the sky. This should even be true for AKARI N(H) maps, as the thermal emission of the interstellar medium is expected to the optically thin at these spatial scales. For a sample of selected regions with Galactic cirrus emission as the dominant source of spatial structure, Kiss et al. (2003) found a power spectral index of $\alpha = -2.3 \pm 0.6$ for ISOPHOT surface brightness maps, while Doi et al. (2015) found a similar value of -2.61 ± 0.01 for AKARI FIS images. This spatial structure is expected for the regions with the faintest backgrounds, typically with an absolute surface brightness of $B \lesssim 2$ MJy sr^{-1} in the far infrared ($100 \leq \lambda \leq 200\,\mu$m), below ∼0.1 arcmin^{-1} spatial frequencies,

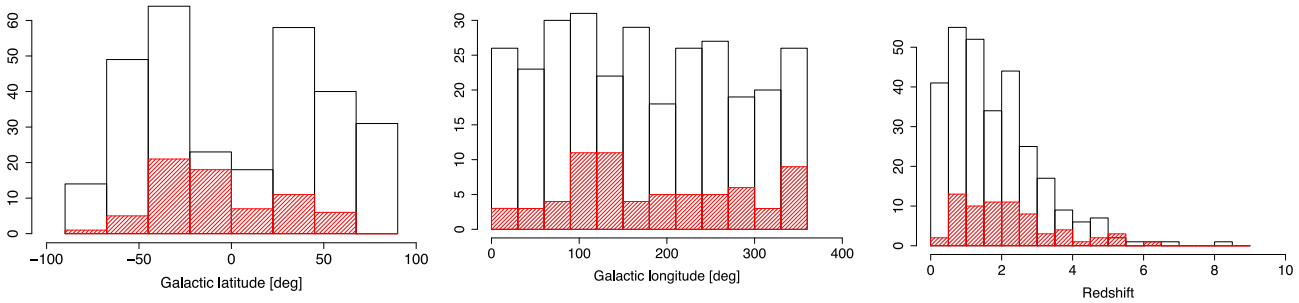

Fig. 6. Galactic latitude, longitude, and redshift distribution for the initial sample (black line) and for the 69 selected sources (red line).

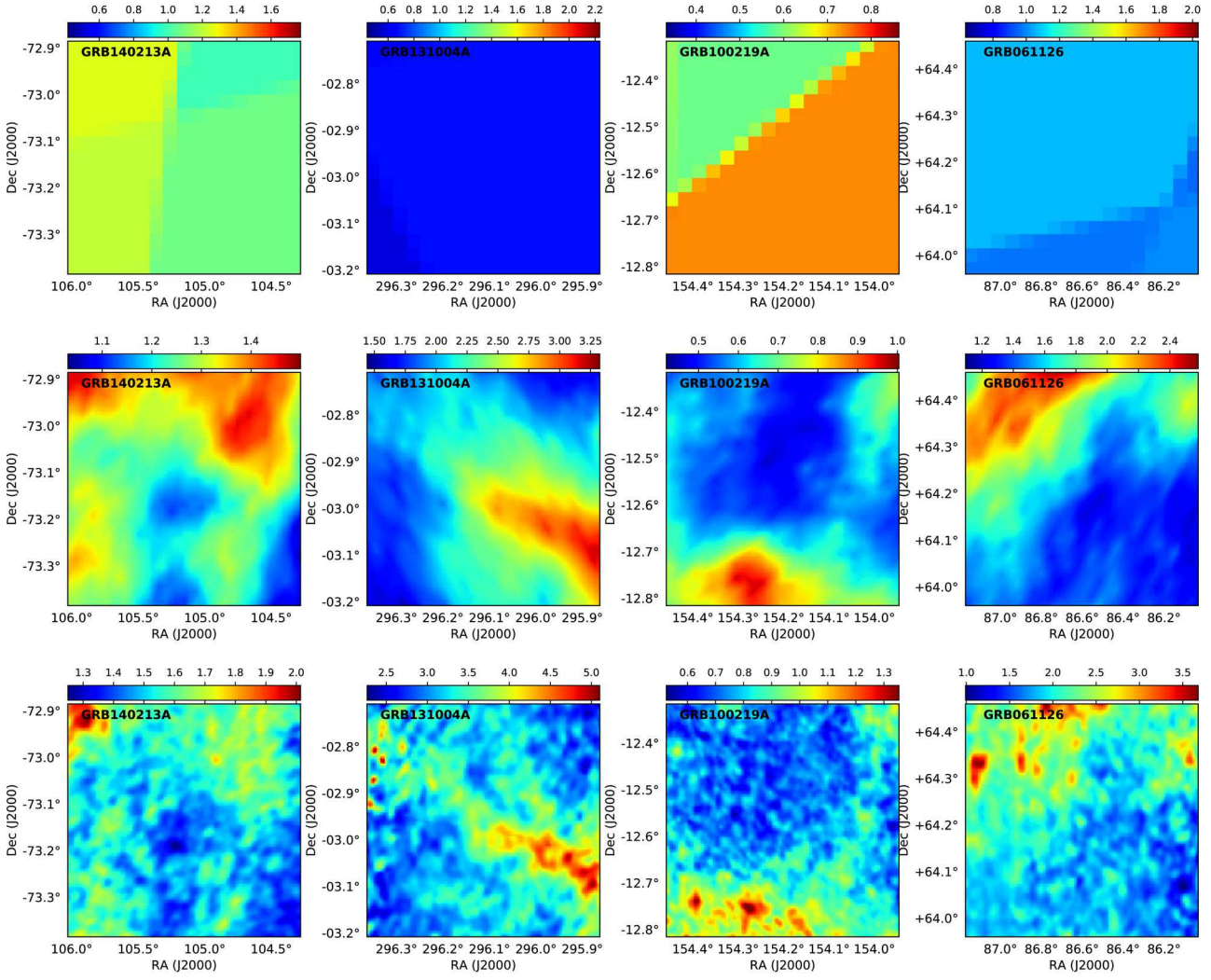

Fig. 7. Galactic foreground column density maps in $10^{21}\,\mathrm{cm}^{-2}$ units in the direction of four of the selected GRBs: GRB140213A, GRB131004A, GRB100219A, and GRB061126 (from left to right), based on LAB (top), Planck PR2 RQ (middle), and calibrated AKARI (bottom) data.

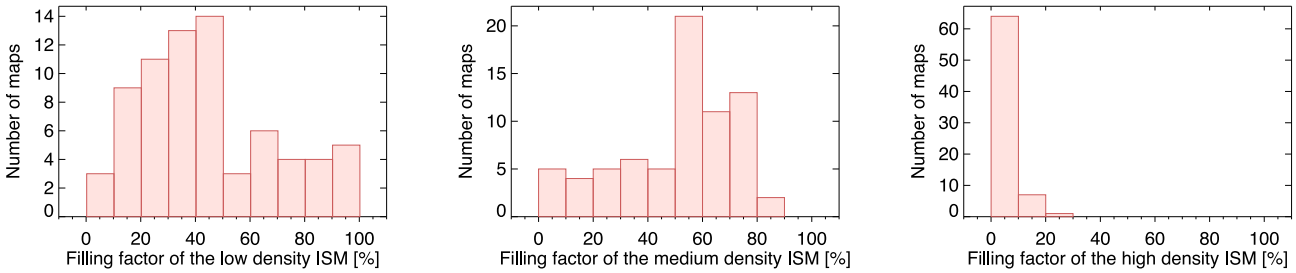

Fig. 8. Filling factor of low (left), medium (middle), and high (right) Galactic foreground column density pixels in the tested AKARI fields. The limits used are 1/3 and 2/3 of the difference between the maximum and minimum in a given field.

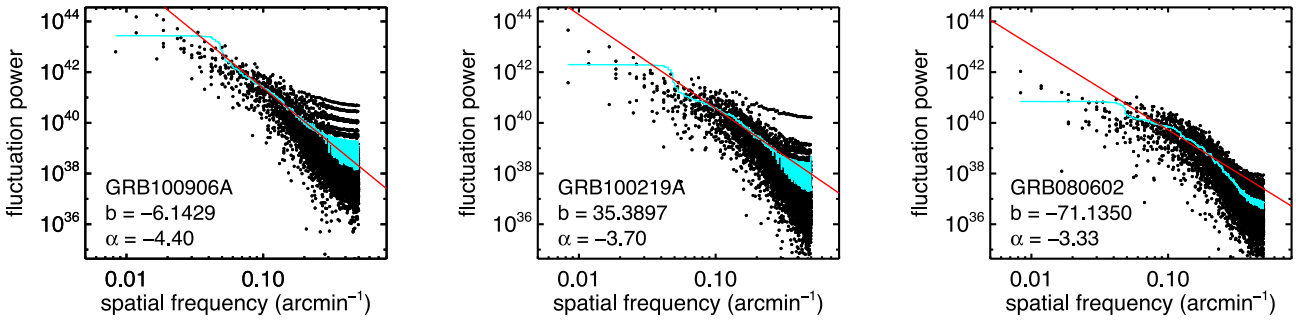

Fig. 9. Power spectra of three sample fields of varying galactic latitudes. Each dot represents an [f, $P(f)$] pair; the blue line is the smoothed average to outline the trend, the red line is the fitted linear. The high frequency end is determined by the Nyquist limit, the low frequency end by the size of the map.

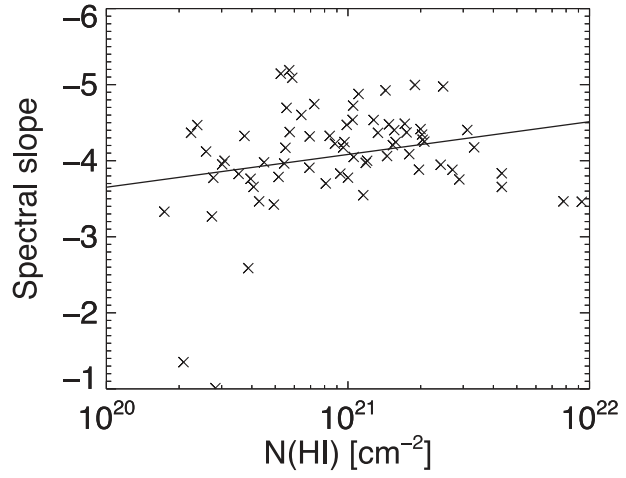

Fig. 10. Relationship of the spectral slope with the average neutral hydrogen column density. The least-squares linear fit is shown.

where the structure noise of the Galactic foreground is dominant over the instrument noise and the extragalactic background fluctuations. Similar power spectra were found for cirrus regions in the sub-millimeter using Herschel SPIRE (Miville-Deschênes et al. 2010) and the BLAST balloon telescope (Roy et al. 2010). As was shown by Kiss et al. (2003), however, the presence of multiple layers, regions with extended emission, and in particular the contribution of dust emission from higher-density (molecular) material, increases the steepness of the power spectra significantly. In Kiss et al. (2003), spectral indices were found up to $\alpha \approx -5$, the most extreme ones in that sample for the Chameleon molecular clouds.

In our present sample the spectral slopes typically lie in the range $-5 \leq \alpha \leq -2$, very similar to the range found by Kiss et al. (2003) for ISOPHOT maps. They also show a weak dependence on the neutral hydrogen column density—fields with higher H I column density usually have a steeper power spectrum (figure 10). The shallow slopes of $\alpha > -2$ found for a few maps are due to the high Poissonian fluctuation (noise) level at high spatial frequencies in those cases. As demonstrated in figure 9, the spectral index gets shallower with increasing Galactic latitude, as is expected due to the decreasing amount of interstellar medium in the line of sight, along with the vanishing of molecular material.

3.4 Intrinsic column densities

Table 2 contains the intrinsic column density values derived from the XRT analysis using various foreground estimates: the Leicester tables, Planck PR2 RQ, and calibrated AKARI. We also present the duration of the gamma-ray emission measured by the T90 value, and the type of the GRB for the 69 selected GRBs. While the values obtained are typically similar irrespective of the selection of the data set to calculate the Galactic foreground, we also see significant differences. The first obvious fact is that $N(\mathrm{H})_{\mathrm{int}}$ is often

Table 2. Intrinsic column density $N(H)_{int}$ values calculated using Leicester.

ID	$N(H)_{int}$ [10^{20} cm^{-2}]			T90	Type
	Leicester	Planck RQ	AKARI	[s]	
GRB050219A	<0.01	3.07	3.15	23.7	L
GRB050223	<0.01	<0.01	<0.01	22.5	L
GRB050318	9.67	12.86	11.34	32	L
GRB050730	38	35.22	30.33	156.5	L
GRB050820A	33	63.33	52.07	26	L
GRB050904	200	318.51	597.43	174.2	L
GRB051022	570	558.96	556.77	200	L
GRB051109A	<0.01	154.21	138.73	37.2	L
GRB051111	58	44.61	47.1	46.1	L
GRB060124	51	74.24	49.22	750	L
GRB060729	7.63	8.28	6.39	115.3	L
GRB061126	10	58.69	41.29	70.8	L
GRB061202	1590	1705.08	1705.86	91.2	L
GRB061222A	510	571.41	576.22	71.4	L
GRB070306	360	357.61	349.35	209.5	L
GRB070328	260	258.62	238.96	75.3	L
GRB070419B	80	108.3	103.7	236.4	L
GRB070714B	55	54.73	47.47	64	L
GRB071020	13	31.7	50.18	4.21	I
GRB071025	370	530.06	595.64	109	L
GRB080319C	91	86.42	88.27	34	L
GRB080602	150	164.37	166.51	74	L
GRB080721	80	90.18	79.33	16.2	L
GRB080928	36	51.16	49.02	280	L
GRB081029	72	101.35	105.76	270	L
GRB090201	1050	1036.71	1029.82	83	L
GRB090205	36	111.1	201.6	8.8	L
GRB090418A	160	161.6	156.56	56	L
GRB090618	24	22.91	25.23	113.2	L
GRB090809	95	114.14	158.45	5.4	I
GRB091024	410	319.14	320.73	109.8	L
GRB100219A	<0.01	105.3	98.24	18.8	L
GRB100606A	21	160.51	164.03	480	L
GRB100728A	240	255.52	269.7	198.5	L
GRB100728B	63	81.1	92.78	12.1	L
GRB100901A	31	41.05	49.25	439	L
GRB100906A	51	85.45	108.69	114.4	L
GRB101225A	15	22.14	27.26	1088	L
GRB110213A	6.15	65.66	74.31	48	L
GRB110715A	160	132.09	123.21	13	L
GRB110818A	140	158.64	156.6	103	L
GRB111107A	<0.01	6.82	12.22	26.6	L
GRB111123A	18	472.88	460.17	290	L
GRB111228A	35	35.63	37.35	101.2	L
GRB111229A	41	47.48	31.18	25.4	L
GRB120118B	570	434.78	375.63	23.3	L
GRB120326A	44	60.24	62.18	69.6	L
GRB120404A	64	73.67	85.1	38.7	L
GRB120729A	25	45.61	45.77	71.5	L
GRB120802A	84	195.47	190.74	50	L
GRB120811C	120	113.24	101.07	26.8	L
GRB120907A	16	17.43	15.67	16.9	L
GRB120909A	250	323.87	319.19	63.3	L
GRB121024A	110	130.54	137.49	69	L
GRB121128A	54	152.87	131.44	23.3	L
GRB130701A	19	31.48	28.53	4.4	I
GRB130702A	5.76	5.17	4.84	59	L
GRB130907A	110	108.83	108.07	>360	L
GRB131004A	65	27.43	33.52	1.54	S
GRB131227A	52	1850.56	2685.37	18	L
GRB140206A	190	135.05	90.96	93.6	L
GRB140213A	12	36.66	39.92	60	L
GRB140304A	420	530.61	496.31	15.6	L
GRB140430A	82	131.2	142.43	173.6	L
GRB140506A	87	93.25	95.1	111.1	L
GRB140614A	150	275.31	237.62	720	L
GRB140703A	100	208.32	186.14	67.1	L
GRB141004A	4.62	29.66	26.74	3.92	I
GRB150403A	80	101.8	104.26	40.9	L

*Planck RQ and AKARI-based galactic foreground column densities. For $N(H)_{int} < 10^{18}$ cm^{-2} only an upper limit is given. We also list the duration of the gamma-ray emission as measured by the T90 value, and the type (S: short; I: intermediate; L: long) of the GRB for the 69 selected GRBs.

higher, and very rarely lower for higher-resolution foreground definition. This can easily be explained by the low filling factor of high column density regions. The $N(H)_{int}$ values are also compared in figure 11.

Figure 11 shows the correlation between the calculated $N(H)_{int}$ intrinsic hydrogen column density values based on the LAB, Planck RQ, and AKARI data. We restricted the plots to $N(H)_{int} > 10^{19}$ cm^{-2}. The five GRBs which are missing from these figures due to their very low intrinsic column density values will be discussed in subsection 4.2.

4 Discussion

4.1 The effect of resolving foreground structures

The attempt to use the high-resolution AKARI FIS all-sky survey FIR data defining the Galactic foreground of extragalactic sources was successful. Our AKARI-based maps of the Galactic foreground column density show a variety of structures formerly unresolved. Accordingly, our new $N(H)_{Gal}$ values are often different, i.e., smaller or higher than is assumed by the former estimates based on the LAB survey. In general we may recommend the use of AKARI-based foreground estimation for all extragalactic uses. Specifically for the purpose of a better estimate of GRB parameters, the improvement in resolving the foreground looks significant.

The AKARI-based foreground column densities were more often smaller rather than larger compared to the LAB-survey-based ones. Not surprisingly, usually (in 49 cases out

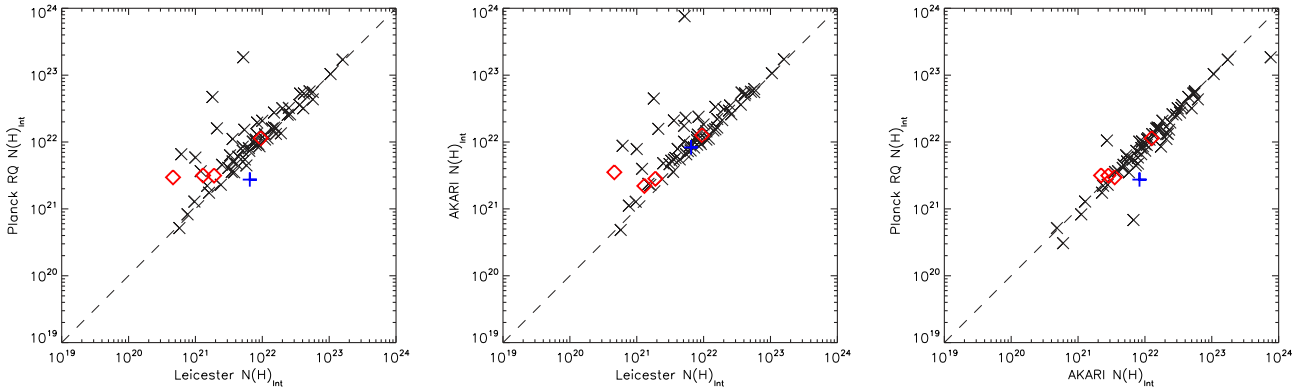

Fig. 11. Correlation of the calculated $N(H)_{Int}$ intrinsic column densities, for the cases where $N(H)_{int} > 10^{18}\,cm^{-2}$ (see table 2). Left: Planck second public release RQ vs. Leicester. Middle: AKARI vs. Leicester. Right: Planck second public release RQ vs. AKARI. Blue plus signs, red diamonds, and crosses indicate the short, intermediate, and long GRBs, respectively. The dashed line shows the line of identity.

of 73) the new AKARI-FIS-based $N(H)_{int}$ values are larger than the old ones based on the LAB survey, as also seen in figure 11 (middle). On the other hand, the resulting change in the intrinsic column densities is typically not larger than the relatively large uncertainty of the $N(H)_{int}$ estimation from the XRT fits of the X-ray spectra. That is actually similar to the one-sigma deviations from the line of identity in figure 11 (middle). For two of those sources, however, the increase is over $10^{23}\,cm^{-2}$ (see also the next subsection). The $N(H)_{int}$ value decreased in 24 cases, but always within the range of the fit errors.

As demonstrated above, fluctuations due to foreground structures have a very important effect on the foreground determination of distant sources. This is even true at spatial frequencies higher than are available with AKARI measurements. In a recent paper, Klaas et al. (2018) showed that secondary standard stars of the PACS instrument of the Herschel Space Observatory may show false far-infrared (especially 160 μm) excess due to the presence of background fluctuations/confusion even at the $\sim 10''$ spatial scale, notably below the AKARI spatial resolution. This led to a reconsideration of the secondary standard star list of Herschel/PACS, and of future far-infrared instruments.

4.2 Non-enveloped GRBs

A special motivation of our project was to investigate the extremely low intrinsic column densities often found in the LAB-based Leicester catalogue. We call the $N(H)_{int} < 10^{18}\,cm^{-2}$ GRBs "non-enveloped," referring to the missing ISM cover. We note that, according to the Leicester analysis, there are as many as 53 non-enveloped GRBs (about one in seven) among the 328 SWIFT XRT GRBs with known spectroscopic redshifts, as is also seen in figure 1. Most of these non-enveloped GRBs are long GRBs (LGRBs), for which the progenitors were thought to be very massive stars, and thus short-lived objects in massive star-forming regions. Thus one would expect a reasonable amount of ISM surrounding the progenitors, and then the GRB as well.

We have five non-enveloped GRBs based on the Leicester analysis among the 69 selected: GRB050219A, GRB050223, GBR051109A, GRB100219A, and GRB111107A—approximately 1 in 14. Thus our investigations barely sample the population of the Leicester non-enveloped LGRBs. The calibrated AKARI foreground hydrogen column density maps are shown with 2′ resolution in the Appendix. Checking the above five directions, we see that all except GRB050223 has a low column density region in the centre (i.e., in the direction of the GRB). The "hole" is quite small in the direction of GRB111107A, and extended for the other three. That explains why the AKARI-based $N(H)_{Gal}$ values are smaller than the low-resolution LAB-survey-based ones, which average up the higher column densities in the surroundings with the lower column density at the middle parts. Correspondingly applying the AKARI-based foreground estimates, only one GRB remained non-enveloped out of the five. That one is GRB050223, an LGRB with a T90 value of 22.5 s.

Figure 12 shows the galactic foreground hydrogen column density distribution in the direction of GRB050223, based on the all-sky surveys at different resolutions.

All the estimates indicate a similar $N(H)_{Gal}$; thus, we must conclude that GRB050223 is indeed a non-enveloped LGRB.

4.3 Redshift dependence of $N(H)_{int}$

Grupe et al. (2007) investigated the redshift dependence of the intrinsic hydrogen column density for GRBs. From

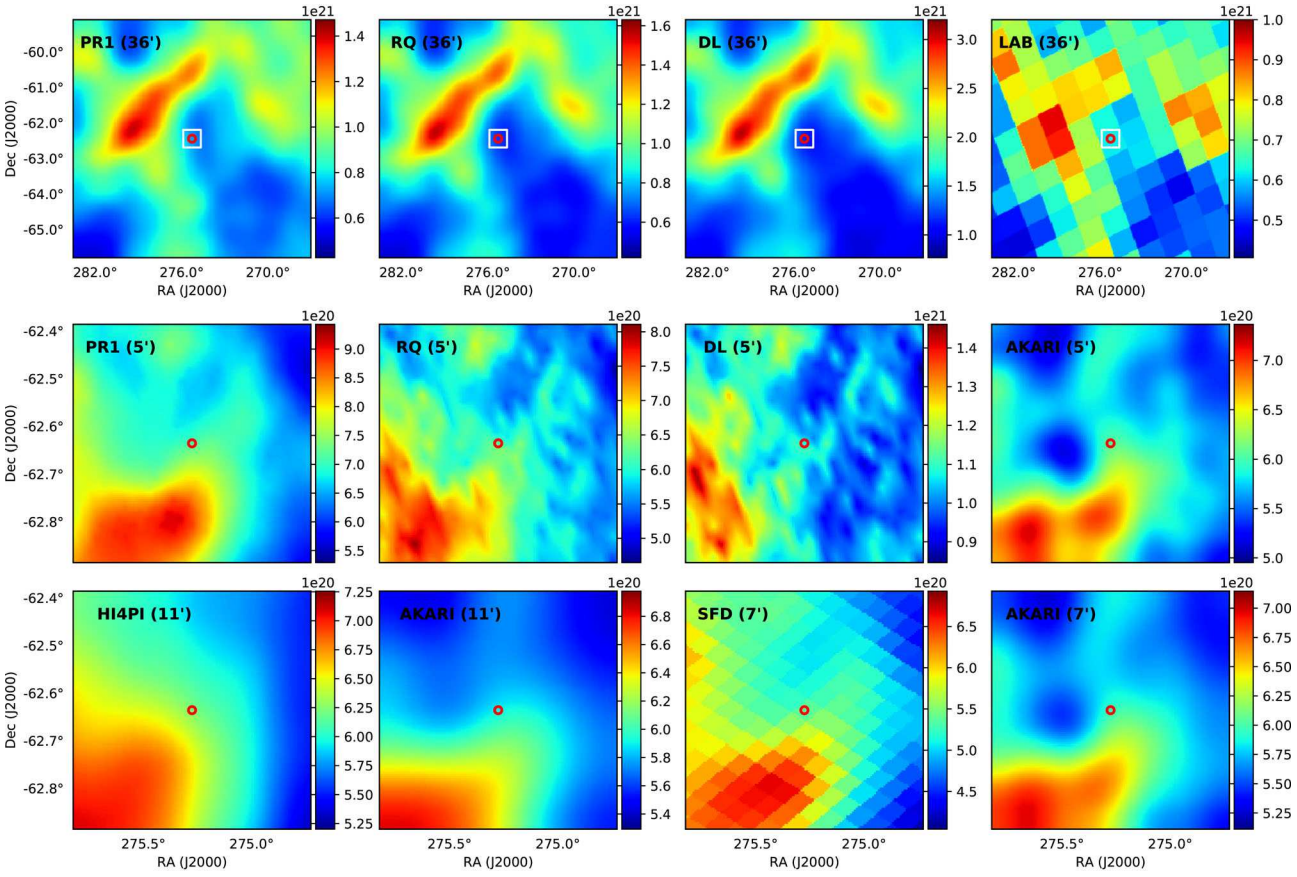

Fig. 12. Galactic foreground hydrogen column density distribution in the direction of GRB050223, based on various all-sky surveys. First row: The first three images from the left are Planck PR1, Planck PR2 RQ, and Planck PR2 DL based $N(\mathrm{H})_{\mathrm{Gal}}$ distributions smoothed to 36′ resolution; the right one is $N(\mathrm{H})_{\mathrm{Gal}}$ from the LAB survey. Second row: All the images show the central area of the top row (marked with a white box), but with a resolution of 5′. The first three images from the left are similar to the first row; the left one is based on AKARI FIS data. Third row: The first two from the left are $N(\mathrm{H})_{\mathrm{Gal}}$ with 11′ resolution based on EBHIS and AKARI. The right two are based on SFD and AKARI, both with 7′ resolution. See also text.

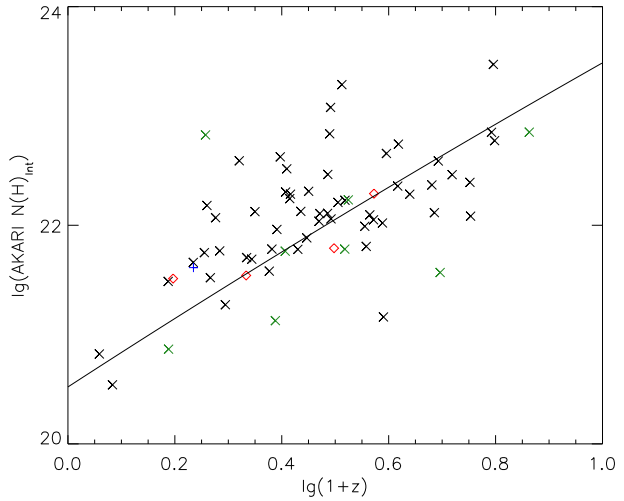

Fig. 13. Intrinsic hydrogen column density as a function of the redshift for the selected GRBs, except GRB050223. Blue plus signs, red diamonds, and crosses indicate the short, intermediate, and long GRBs, respectively. Green crosses mark the eight GRBs from Grupe et al. (2007). A least-squares linear fit is over-plotted.

a sample of 56 GRBs, they concluded that high-redshift bursts more often show low $[N(\mathrm{H})_{\mathrm{int}} < 10^{21}\,\mathrm{cm}^{-2}]$ values. We note that their analysis of the XRT spectra was the same as ours except that they used an earlier version of the reduction software, and a very low-resolution foreground column density input from Dickey and Lockman (1990). Our result on the comparison of redshifts and $N(\mathrm{H})_{\mathrm{int}}$ is shown in figure 13, using the same symbols as in figure 11. There are eight sources common to the samples of Grupe et al. (2007) and ours, which are marked in green.

There is a clear redshift dependence seen using the AKARI-FIS-based foreground estimates. The least-squares fitted slope is around 2, which corresponds to the Born approximation (Born 1926a, 1926b). See more details on this issue in Racz and Hortobagyi (2018).

5 Conclusions and future investigations

The AKARI-FIS-based foreground hydrogen column density estimates typically agree fairly well with the LAB-survey-based values in the Leicester archive, but also are

typically slightly smaller. This is mainly due to the fact that the filling factor of the low column densities is higher than the high columnm density ones. As a result, the intrinsic hydrogen column densities are typically slightly higher when calculated using an AKARI-based foreground.

We note that there are a few directions where there is a significant difference between the low-resolution previous and our new AKARI-based foreground values, and as a consequence the number of extremely low and high intrinsic column densities is reduced.

We drew our conclusions using a fraction of the available AKARI FIS data; with a new version of the all-sky maps, one might increase the number of regions studied and include several more GRBs. We have seen the relatively low filling factor of high column density directions at various galactic latitudes. That should be further investigated with appropriate statistical methods. It is a challenge to estimate the hydrogen column density from dust emission. At high galactic latitudes one may actually measure the H I 21 cm emission in high resolution using interferometry and also observing continuum sources in the background, which allows an estimate of the optical depth. At lower galactic latitudes molecular line measurements should be included, such as OH, CH, and/or CO, to also calculate the H_2 column density.

There are a few LGRBs with challenging low intrinsic hydrogen column densities. One should examine their nature to understand the lack of surrounding dense ISM. We also note that the population of candidate non-enveloped LGRBs in figure 1 includes further interesting objects, like, for example, GRB080310 and GRB100425A, with high redshift values of $z = 2.427$ (Fox et al. 2008) and $z = 1.755$ (Goldoni et al. 2010), respectively. But those were not included in our current detailed AKARI-based analysis due to the lower correlation of their Planck-based and AKARI-based $N(\mathrm{H})_{\mathrm{Gal}}$ data. Such directions should be tested, e.g., using new AKARI FIS data.

Acknowledgment

This research was supported by Hungarian OTKA grant NN111016. This work made use of data supplied by the UK Swift Science Data Centre at the University of Leicester. Y.D. has been supported by Grants-in-Aid for Scientific Research (25247016, 18H01250). C.K. has been supported by the Hungarian National Research, Development and Innovation Office (NKFIH), grant K-125015, and by the European Union's Horizon 2020 Research and Innovation Programme, under Grant Agreement no. 687378, "Small Bodies: Near and Far." The authors acknowledge the useful comments from the anonymous referee.

Supplementary date

The following supplementary data are available at *PASJ* online.

$N(\mathrm{H})_{\mathrm{Gal}}$ maps for all the selected sources.
Galactic foreground hydrogen column density distributions in the direction of the selected GRBs (GRB050730, GRB050820A, GRB050904, and GRB051022), based on various all-sky surveys. Left row: The first three images from the top are Planck PR1, Planck PR2 RQ, and Planck PR2 DL based $N(\mathrm{H})_{\mathrm{Gal}}$ distributions smoothed to 36′ resolution; the bottom one is $N(\mathrm{H})_{\mathrm{Gal}}$ from the LAB survey. Middle row: All the images show the central area of the left column (marked with a white box), but with a resolution of 5′. The first three images from the top are similar to the left column; the bottom one is based on AKARI FIS data. Right row: The first two from the top are $N(\mathrm{H})_{\mathrm{Gal}}$ with 11′ resolution based on EBHIS and AKARI. The lower two are based on SFD and AKARI, both with 7′ resolution.

Appendix. AKARI-based $N(\mathrm{H})_{\mathrm{Gal}}$ maps for all the selected sources

In order to display the variety of foreground patterns, and to help future follow-ups, we present here the calibrated AKARI-based $N(\mathrm{H})_{\mathrm{Gal}}$ Galactic hydrogen column density maps in the direction of all 69 selected GRBs with 2′ resolution (figure 14).

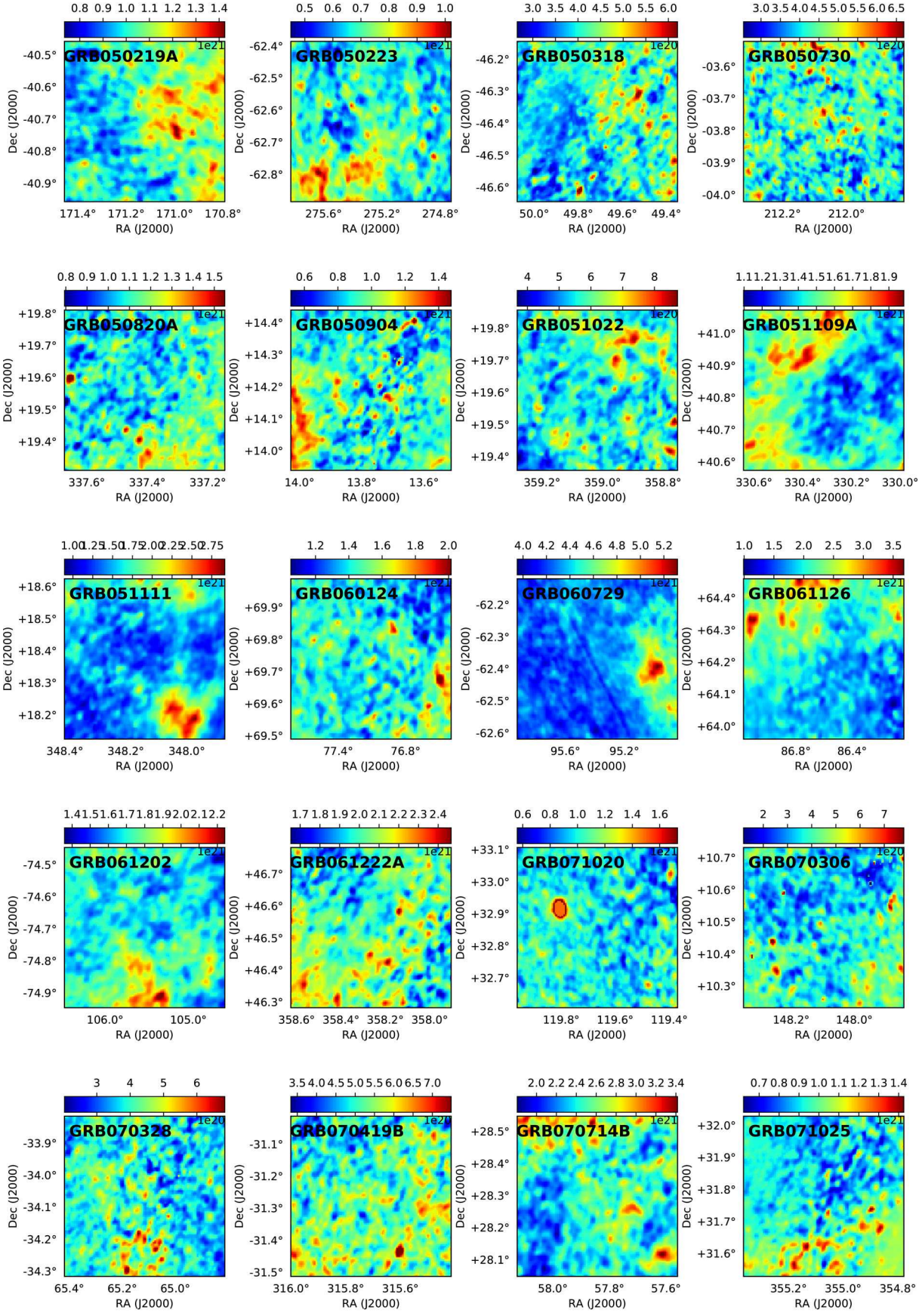

Fig. 14. Calibrated AKARI-based column density maps in the direction of the selected GRBs with 2′ resolution.

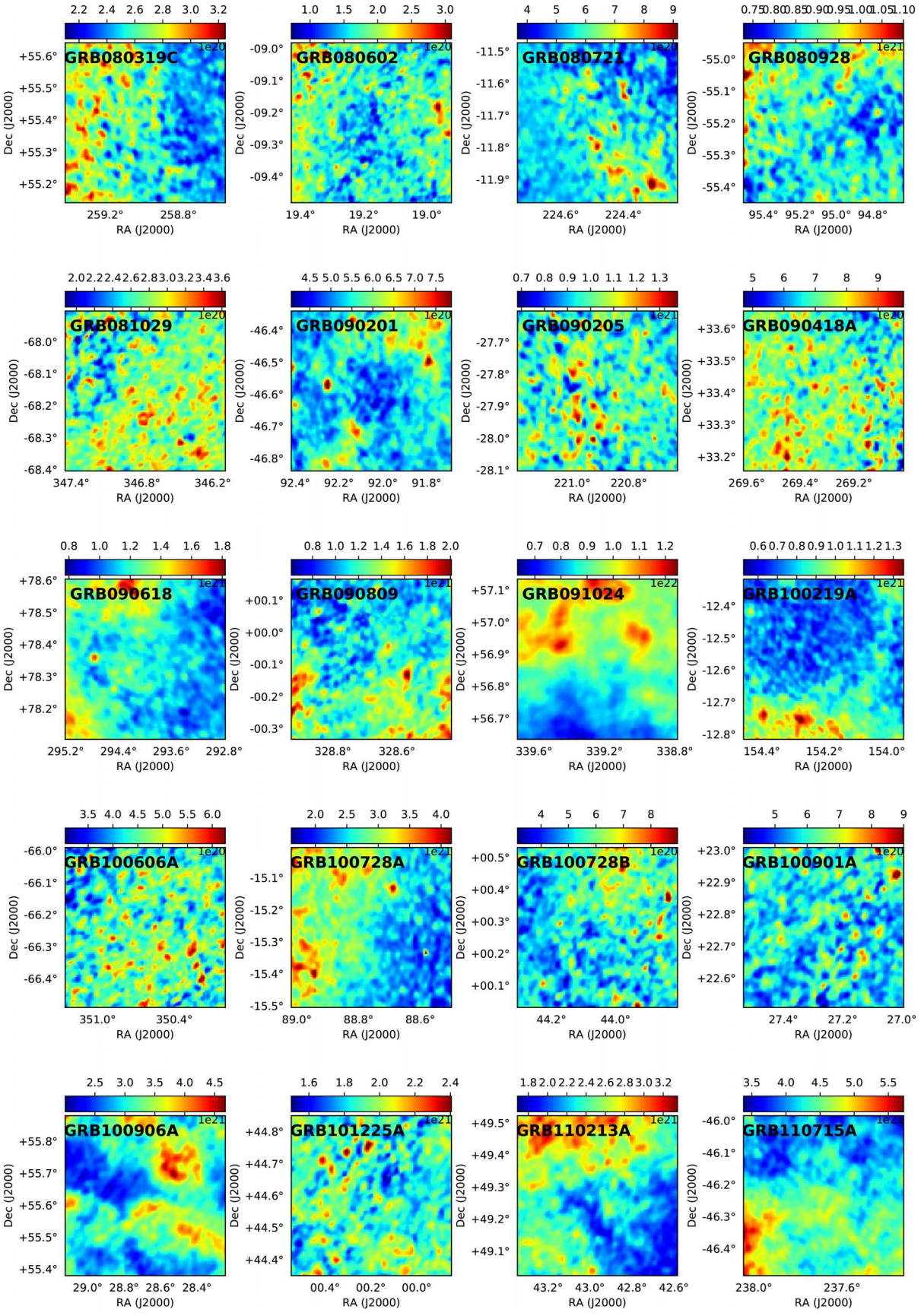

Fig. 14. (Continued)

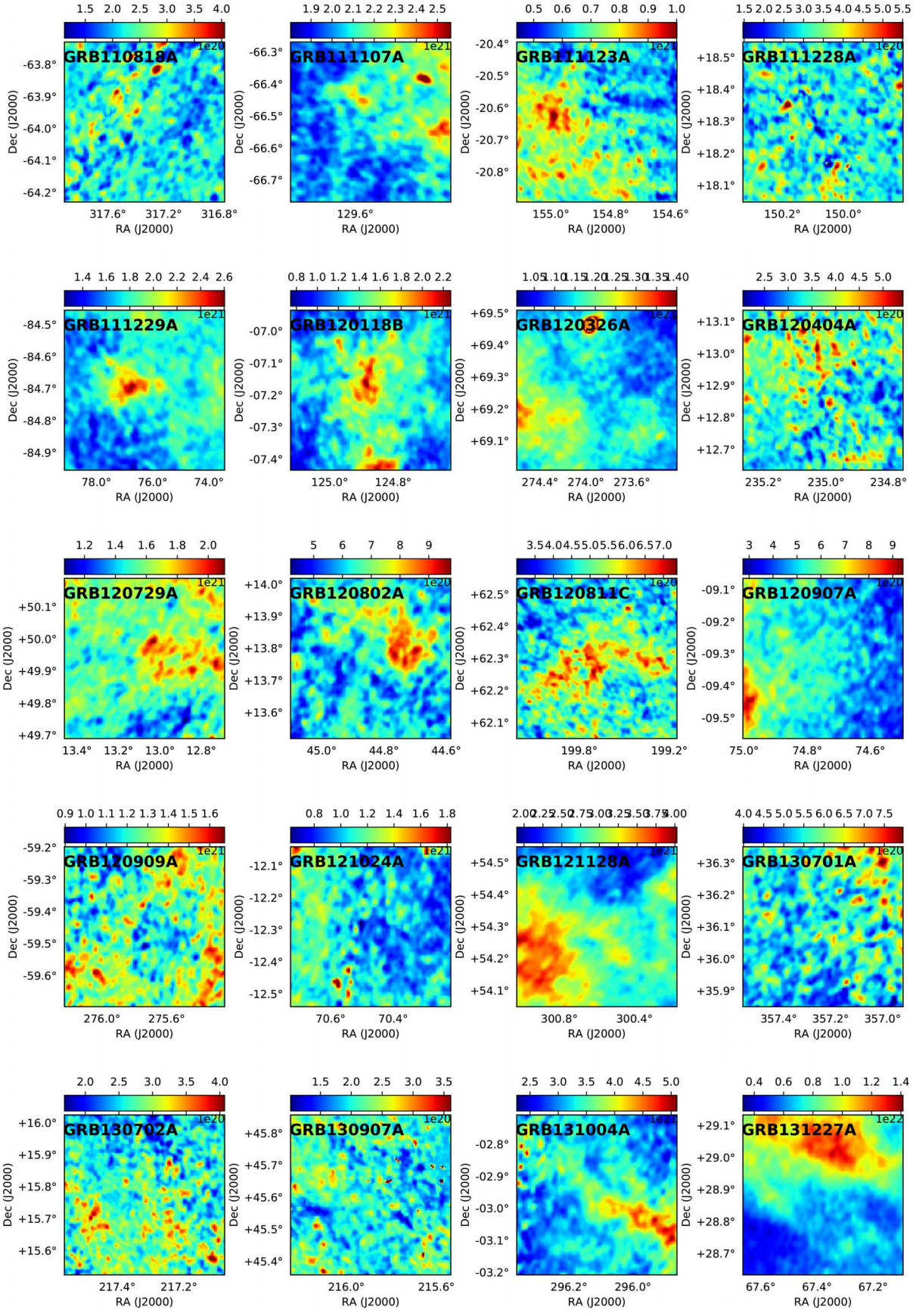

Fig. 14. (Continued)

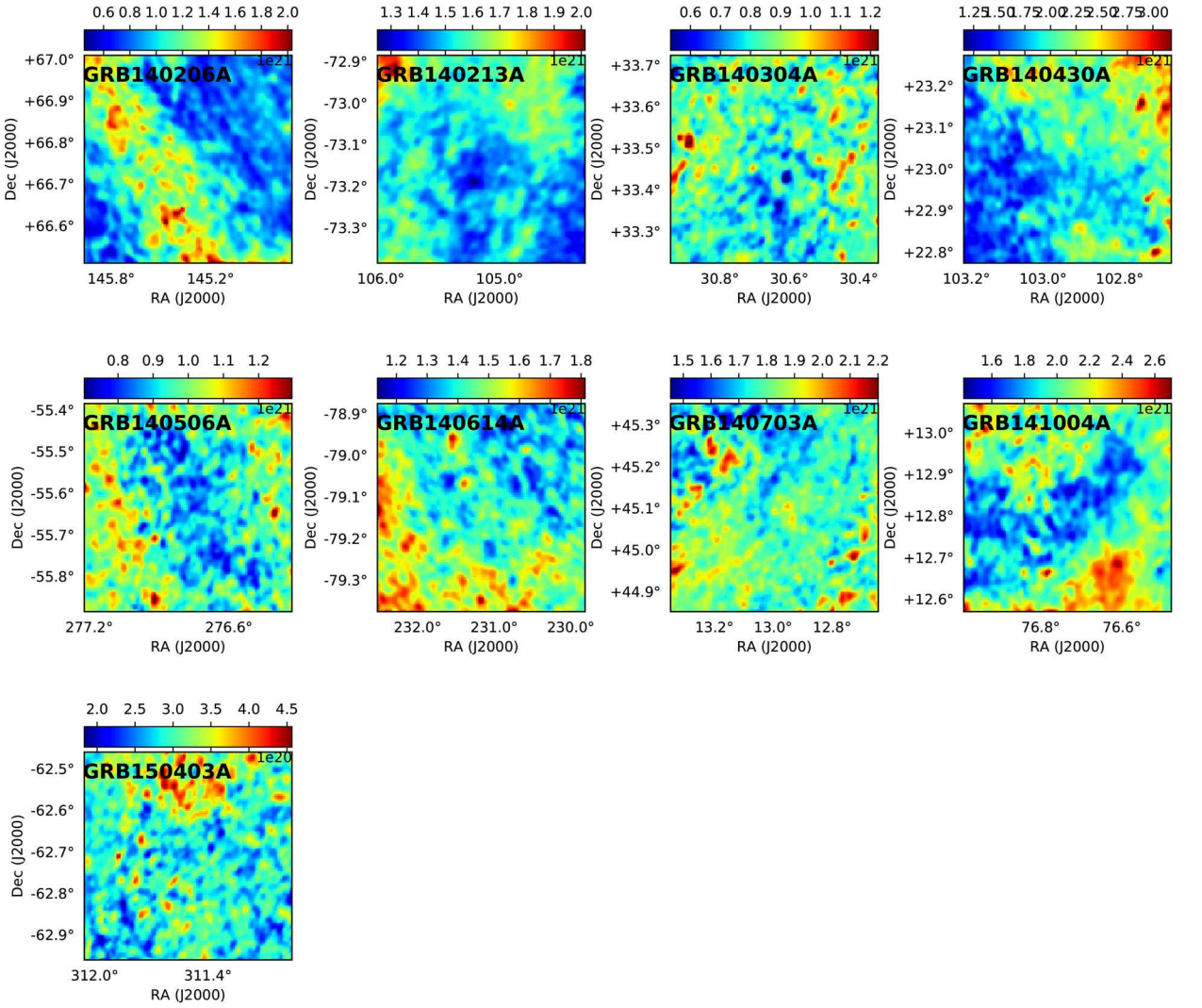

Fig. 14. (Continued)

References

Arnaud, K. A. 1996, ASP Conf. Ser., 101, 17

Bagoly, Z., Horváth, I., Hakkila, J., & Tóth, L. V. 2016, in IAU Symp. 319, Galaxies at High Redshift and Their Evolution Over Cosmic Time, ed. S. Kaviraj (Cambridge: Cambridge University Press), 2

Balázs, L. G., Bagoly, Z., Hakkila, J. E., Horváth, I., Kóbori, J., Rácz, I. I., & Tóth, L. V. 2015, MNRAS, 452, 2236

Behar, E., Dado, S., Dar, A., & Laor, A. 2011, ApJ, 734, 26

Bevington, P. R. 1969, Data Reduction and Error Analysis for the Physical Sciences (New York: McGraw-Hill)

Boër, M., Gendre, B., & Stratta, G. 2015, ApJ, 800, 16

Born, M. 1926a, Z. Phys., 37, 863

Born, M. 1926b, Z. Phys., 38, 803

Burstein, D., & Heiles, C. 1982, AJ, 87, 1165

Campana, S., et al. 2012, MNRAS, 421, 1697

Dickey, J. M., & Lockman, F. J. 1990, ARA&A, 28, 215

Dobashi, K., Uehara, H., Kandori, R., Sakurai, T., Kaiden, M., Umemoto, T., & Sato, F. 2005, PASJ, 57, S1

Doi, Y., et al. 2012, Publ. Korea Astron. Soc., 27, 111

Doi, Y., et al. 2015, PASJ, 67, 50

Dorman, B., & Arnaud, K. A. 2001, ASP Conf. Ser., 238, 415

Elíasdóttir, Á., et al. 2009, ApJ, 697, 1725

Elliott, J., et al. 2013, A&A, 556, A23

Evans, P. A., et al. 2009, MNRAS, 397, 1177

Fox, A. J., Ledoux, C., Vreeswijk, P. M., Smette, A., & Jaunsen, A. O. 2008, A&A, 491, 189

Fynbo, J. P. U., et al. 2009, ApJS, 185, 526

Goldoni, P., Flores, H., Malesani, D., Levan, A. J., Tanvir, N. R., & Fynbo, J. P. U. 2010, GCN Circ., 10684

Gomboc, A. 2012, Contemp. Phys., 53, 339

Grupe, D., Nousek, J. A., vanden Berk, D. E., Roming, P. W. A., Burrows, D. N., Godet, O., Osborne, J., & Gehrels, N. 2007, AJ, 133, 2216

Güver, T., & Özel, F. 2009, MNRAS, 400, 2050

HI4PI Collaboration, 2016, A&A, 594, A116

Horváth, I. 2009, Ap&SS, 323, 83

Horváth, I., Bagoly, Z., Hakkila, J., & Tóth, L. V. 2015, A&A, 584, A48

Horváth, I., & Tóth, B. G. 2016, Ap&SS, 361, 155

Hunt, L. K., et al. 2014, A&A, 565, A112
Kalberla, P. M. W., Burton, W. B., Hartmann, D., Arnal, E. M., Bajaja, E., Morras, R., & Pöppel, W. G. L. 2005, A&A, 440, 775
Kawada, M., et al. 2007, PASJ, 59, S389
Kiss, C., Ábrahám, P., Klaas, U., Lemke, D., Héraudeau, P., del Burgo, C., & Herbstmeier, U. 2003, A&A, 399, 177
Klaas, U., Balog, Z., Nielbock, M., Müller, T. G., Linz, H., & Kiss, C. 2018, A&A, 613, A40
Kohyama, T., Shibai, H., Fukagawa, M., & Sumi, T. 2013, PASJ, 65, 13
Kouveliotou, C., Meegan, C. A., Fishman, G. J., Bhat, N. P., Briggs, M. S., Koshut, T. M., Paciesas, W. S., & Pendleton, G. N. 1993, ApJ, 413, L101
Kumar, P., & Zhang, B. 2015, Phys. Rev., 561, 1
Lemke, D., et al. 1996, A&A, 315, L64
Lynds, B. T. 1965, ApJS, 12, 163
McClure-Griffiths, N. M., et al. 2009, ApJS, 181, 398
Mészáros, P., & Rees, M. J. 1997, ApJ, 476, 232
Miville-Deschênes, M.-A., et al. 2010, A&A, 518, L104
Murakami, H., et al. 2007, PASJ, 59, S369
Nakagawa, T., et al. 2007, PASJ, 59, S377
Neugebauer, G., et al. 1984, ApJ, 278, L1
Ootsubo, T., et al. 2016, PASJ, 68, 35
Planck Collaboration, 2014a, A&A, 571, A1
Planck Collaboration, 2014b, A&A, 571, A11
Planck Collaboration, 2016, A&A, 586, A132
Press, W. H., Teukolsky, S. A., Vetterling, W. T., & Flannery, B. P. 1992, Numerical Recipes in FORTRAN, 2nd ed. (Cambridge: Cambridge University Press)
Price, P. A., et al. 2002, ApJ, 571, L121
Racz, I. I., & Hortobagyi, A. J. 2018, AN, in press
Roy, A., et al. 2010, ApJ, 708, 1611
Sari, R., Piran, T., & Narayan, R. 1998, ApJ, 497, L17
Schady, P. 2015, J. High Energy Astrophys., 7, 56
Schady, P., et al. 2014, A&A, 570, A52
Schady, P., et al. 2015, A&A, 579, A126
Schady, P., Savaglio, S., Krühler, T., Greiner, J., & Rau, A. 2011, A&A, 525, A113
Schlafly, E. F., & Finkbeiner, D. P. 2011, ApJ, 737, 103
Schlegel, D. J., Finkbeiner, D. P., & Davis, M. 1998, ApJ, 500, 525
Stanek, K. Z., et al. 2003, ApJ, 591, L17
Starling, R. L. C., Willingale, R., Tanvir, N. R., Scott, A. E., Wiersema, K., O'Brien, P. T., Levan, A. J., & Stewart, G. C. 2013, MNRAS, 431, 3159
Totani, T., et al. 2014, PASJ, 66, 63
Verner, D. A., Ferland, G. J., Korista, K. T., & Yakovlev, D. G. 1996, ApJ, 465, 487
Wang, J. 2013, ApJ, 776, 96
Watson, D. 2011, A&A, 533, A16
Willingale, R., Starling, R. L. C., Beardmore, A. P., Tanvir, N. R., & O'Brien, P. T. 2013, MNRAS, 431, 394
Wilms, J., Allen, A., & McCray, R. 2000, ApJ, 542, 914
Winkel, B., Kerp, J., Flöer, L., Kalberla, P. M. W., Ben Bekhti, N., Keller, R., & Lenz, D. 2016, A&A, 585, A41
Wiseman, P., Schady, P., Bolmer, J., Krühler, T., Yates, R. M., Greiner, J., & Fynbo, J. P. U. 2017, A&A, 599, A24
Woosley, S. E., & Bloom, J. S. 2006, ARA&A, 44, 507
Wright, E. L., et al. 2010, AJ, 140, 1868
Yoon, S.-C., Langer, N., & Norman, C. 2006, A&A, 460, 199
Zafar, T. 2016, Planet. Space Sci., 133, 14
Zafar, T., Watson, D., Fynbo, J. P. U., Malesani, D., Jakobsson, P., & de Ugarte Postigo, A. 2011, A&A, 532, A143
Zhang, B., Lü, H.-J., & Liang, E.-W. 2016, Space Sci. Rev., 202, 3
Zhang, B.-B., et al. 2011, ApJ, 730, 141